Tampere University

Truong Nguyen Tuan Minh

DEVELOPMENT OF BIOPHOTONIC SCAFFOLDS FOR INFECTION ERADICATION

Bachelor of Science Thesis
Faculty of Engineering and Natural Sciences
Examiners: PhD Virginia Alessandra Gobbo,
PhD Nirajan Ohja,
Prof. Laeticia Petit
October 2025

ABSTRACT

Minh Truong: Development of biophotonic scaffolds for infection eradication
Bachelor of science thesis
Tampere University
Bachelor's programme in Science and engineering
October 2025

This thesis investigates the development of biophotonic scaffolds with near-infrared (NIR) rechargeable luminescence for potential biomedical applications, particularly light-triggered antimicrobial therapy and tissue regeneration. The study addresses the challenge of integrating persistent luminescence (PeL) and upconversion (UC) functionalities into bioactive glass scaffolds while preserving their mechanical integrity and optical performance.

Rare-earth-doped UC crystals, including $CaTeO_3$ and $NaNbO_3$, were synthesized via solid-state reactions and optimized for blue emission under 808 nm and 980 nm excitation. These emissions served to charge $SrAl_2O_4$: Eu^{2+}, Dy^{3+} phosphors, which provide long-lasting green afterglow. Structural characterization using X-ray diffraction confirmed successful incorporation of dopants, while optical analyses revealed stronger blue emission in $NaNbO_3$, especially when doped with 15 at% Yb^{3+} and 0.25 at% Tm, compared to $CaTeO_3$.

Composite inks were formulated by combining optimized UC crystals, PeL phosphors, and 1393B20 borosilicate bioactive glass. Although nozzle clogging limited successful 3D printing, sintered ink samples displayed visible green afterglow following NIR excitation, confirming that UC emission effectively recharged PeL phosphors. However, the trade-off between luminescent performance and mechanical stability was evident, as $NaNbO_3$-based composites exhibited higher emission but increased brittleness.

The results demonstrate the feasibility of producing multifunctional photonic scaffolds capable of localized light-activated functionality, while highlighting key areas for optimization, including particle size control, ink rheology, and sintering protocols. These findings provide a foundation for future studies focused on enhancing luminescent efficiency, mechanical robustness, and biological performance for clinical translation in regenerative medicine.

Keywords: biophotonic, tissue engineering, persistent luminescence, upconversion, NIR excitation, 3D printing.

PREFACE

This thesis was completed as part of the Bachelor's Programme in Science and Engineering at Tampere University (Tampere, Finland). Most of the experimental work took place during the summer and autumn of 2025 within two research groups: Photonic Glasses (ENS) and Bioceramics, Glasses, and Composites (MET). The writing phase was carried out in the summer and autumn of 2025. The work was supervised by Dr Nirajan Ojha, Dr Virginia Alessandra Gobbo and Professor Laeticia Petit.

I would like to thank Professor Laeticia Petit for her guidance and support throughout my working on the thesis project. Moreover, I would like to thank Dr Nirajan Ojha and the group of Photonic Glasses as well as Dr Virginia Alessandra Gobbo for walking me through my work in the lab and usage of the tools for the research. Additionally, great thanks to Dr Khaldoon Nasser for instructing me from scratch since my first day in the lab.

Lastly, I would like to thank my family for always supporting me all the way despite great distance from my home country.

Thanks all.

Tampere, 22 October 2025

Truong Nguyen Tuan Minh

CONTENTS

LIST OF FIGURES

LIST OF SYMBOLS AND ABBREVIATIONS

θ	Diffraction angle
λ	Wavelength
λ_{exc}	Wavelength of excitation source
3D	Three-dimensional
AM	Additive Manufacturing
A.U.	Arbitrary Unit
d	Spacing between crystals plane
DNICs	Dinitrosyl iron complexes
ECM	Extracellular matrix
HA	Hydroxyapatite
HCA	Hydroxycarbonate apatite
n	Order of diffraction
NIR	Near-infrared
PeL	Persistent luminescence
PGA	Polyglycolic acid
PLLA	poly-L-lactic acid
RE	Rare Earth
RSNOs	S-nitrosothiols
sin	Sine
SNAP	S-Nitroso-N-Acetylpenicillamine
TCP	Tri-calcium phosphate
TE	Tissue Engineering
UC	Upconversion
UV	Ultraviolet
XRD	X-ray diffraction

°	Degree
°C	Degree Celsius
A	Ampere
at%	Atomic percentage
h	Hour (1 h = 3600s)
min	Minute (1 min = 60s)
nm	nanometer (1 nm = 10^{-9} m)
psi	Pounds per square inch (a unit of pressure)
μm	Micrometer (1 μm = 10^{-6} m)
wt%	Weight percentage

B_2O_3	Diboron Trioxide
$CaCO_3$	Calcium Carbonate
CaO	Calcium Oxide
CaO	Calcium Oxide
$CaTeO_3$	Calcium Tellurite
Dy^{3+}	Dysprosium
Er^{3+}	Erbium Ion
Eu^{2+}	Europium Ion
H_3BO_3	Boric Acid
K_2CO_3	Potassium Carbonate
K_2O	Potassium Oxide
MgO	Magnesium Oxide
Na_2CO_3	Sodium Carbonate
Na_2O	Sodium Oxide
Na_2O	Sodium Oxide

$NaNbO_3$	Sodium Niobate
Nd^{3+}	Neodymium
Nd_2O_3	Neodymium(III) Oxide
$NH_4H_2PO_4$	Monoammonium Phosphate
Ni	Nickel
NO	Nitric Oxide
P_2O_5	Diphosphorus Pentoxide
SiO_2	Silicon Dioxide
$SrAl_2O_4$	Strontium Aluminate
TeO_2	Tellurium Dioxide
Tm	Thulium
Tm_2O_3	Thulium(III) Oxide
Yb^{2+}	Ytterbium
Yb_2O_3	Ytterbium(III) Oxide

.

1. INTRODUCTION

Tissue engineering (TE) has emerged as a promising interdisciplinary field that integrates materials science, biology, and engineering to develop functional scaffolds capable of supporting tissue regeneration and repair. The increasing prevalence of traumatic injuries, degenerative diseases, and tumor resections has created a growing demand for biomaterials that can restore or enhance biological function while ensuring structural integrity and limited risk of infection. Among the various approaches, the design of scaffolds that combine mechanical support with advanced functionalities such as bioactivity and photonic response represents a significant step forward in biomedical materials research [Ch, 2002].

Ceramic biomaterials have been widely studied for scaffold fabrication due to their excellent biocompatibility and osteoconductivity. Specifically, some bioactive glasses such as silicate and borosilicate were demonstrated to induce the precipitation of hydroxycarbonate apatite (HCA), when immersed in body fluids, that promotes bone regeneration and increases the bone-material interface stability [OB, 2021]. However, recent developments in photonic biomaterials have opened opportunities for additional therapeutic functions, such as controlled drug delivery, photothermal therapy, and antimicrobial treatment using light as stimulus. In particular, persistent luminescence (PeL) and upconversion (UC) luminescence materials have gained attention for their ability to store and release light energy, enabling excitation deeper within tissues through near-infrared (NIR) light, which is less harmful and penetrates more efficiently than ultraviolet or visible light [Ja, 2012].

Despite their potential, the successful incorporation of UC and PeL phosphors into bioactive scaffolds remains challenging. Factors such as dopant concentration, particle size distribution, and sintering parameters critically influence luminescent performance and mechanical stability. Furthermore, the integration of these materials into three-dimensional (3D) printed scaffolds requires precise formulation to ensure both printability and retention of optical properties after thermal processing.

This thesis investigates the synthesis of UC crystals with Rare Earth (RE) dopants, their combination with PeL phosphors, and their incorporation into bioactive glass matrices to fabricate multifunctional scaffolds. The research aims to evaluate the spectroscopic performance of these composites, providing a foundation for future biomedical applications such as NIR-triggered antimicrobial therapy and tissue regeneration.

2. BACKGROUND

2.1 Scaffold as implant

TE has become a promising strategy for treating damaged or injured tissues. This method relies on a temporary scaffold that provides a surface for cell attachment and acts as structural support to direct the regeneration of the new tissue through physiological pathways [Ch, 2002].

2.1.1 Definition

In biomedical sciences, a scaffold refers to a three-dimensional (3D) porous structure composed of a biocompatible material, created to offer temporary support for cells. It enables cell attachment, growth, movement, and differentiation playing a key role in tissue formation and regeneration [De, 2017].

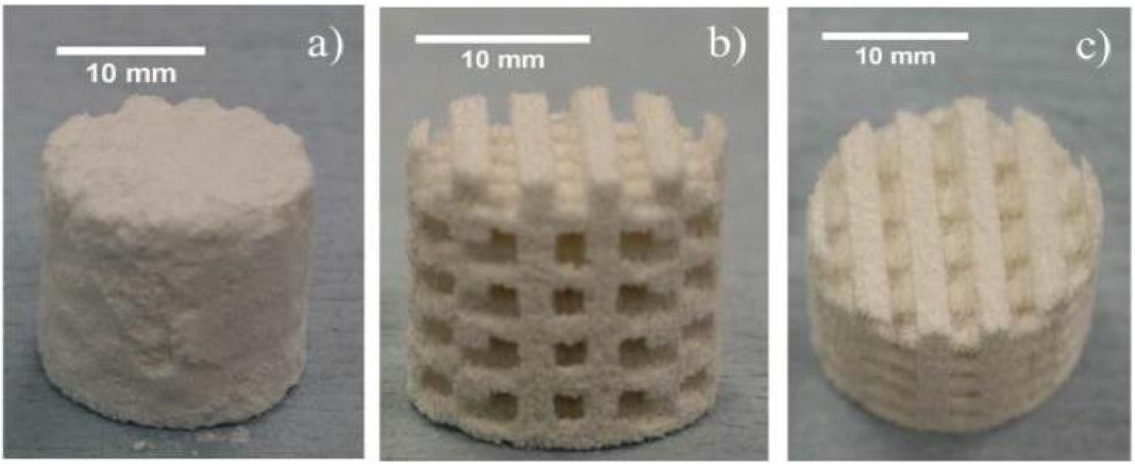

Figure 1: Different structures of scaffold [Co, 2015].

The design of scaffolds (Figure 1) plays a critical role in the success of tissue engineering strategies, as these structures must not only provide temporary physical support but also actively participate in the biological processes that drive tissue regeneration in the aimed physiological way. Therefore, ideal scaffolds for tissue engineering should possess several key features [Ma, 2008]:

- the capacity to interact with cells to promote adhesion, growth, and extracellular matrix (ECM) production;
- a well-connected pore structure that enables efficient cell migration, transport of gases, nutrients, and waste, supporting healthy cell function;

- mechanical strength similar to the target tissue;
- well-integrated to biological system and goodbiocompatibility.

2.1.2 Suitable materials for scaffolds to encourage cellular activity.

Different materials have been applied in scaffolds research, which are metals, natural polymers, synthetic polymers, and bioceramics or bioactive glass (Table 1).

Table 1: Biomaterials for Scaffolds [AI, 2016]

Biomaterials for Scaffolding					
Natural biomaterials		**Synthetic biomaterials**		**Metals**	
Protein origin biomaterials	Polysaccharides origin biomaterials	Polymer biomaterials	Ceramic biomaterials	Biostable metals	Biodegradable metals
Silk Collagen Fibrin Gelatin	Hyaluronan Alginate Agarose Chitosan	Poly-ethylene glycol (PEG) Polyglycolide (PGA) Poly-lactic-co-glycolic acid (PLGA) Poly-D, L-lactide (PDLLA) Poly-e-caprolactone (PCL)	Alumina Zirconia Sintered HA α- or β- tricalcium phosphate (α-TCP, β-TCP) Tetracalcium phosphate Hydroxyapatite Bioactive glass Calcium phosphate	Titanium Stainless steel Cobalt-chromium Tantalum alloys	Magnesium Iron Zinc

Metals are widely explored as biomaterial scaffolds due to their high strength, durability, and biocompatibility, making them suitable for load-bearing applications such as bone and joint repair [AI, 2009]. Titanium, stainless steel, cobalt-chromium, and tantalum alloys are commonly used for permanent implants because of their mechanical stability and corrosion resistance, while biodegradable metals like magnesium, iron, and zinc offer promise for temporary scaffolds that degrade as tissue regenerates [AD, 2024].

Natural polymers used in scaffolds for biomedical tissue engineering mainly include proteins and polysaccharides that closely mimic the native ECM, providing excellent biocompatibility and biodegradability. Common natural polymers consist of collagen, fibrin, silk fibroin, chitosan, and hyaluronic acid. These materials are favored because they provide a biologically recognizable environment that enhances cell attachment, proliferation, and differentiation by mimicking native tissue ECM [Fa, 2022]. They are often processed into hydrogels, fibrous, or porous structures via techniques such as electrospinning, freeze-drying, or 3D printing to meet specific mechanical and biological requirements.

A wide range of synthetic polymers, such as polystyrene, poly-L-lactic acid (PLLA), polyglycolic acid (PGA), and poly-DL-lactic-co-glycolic acid (PLGA), have been explored for scaffold fabrication. Due to their well-defined and highly reproducible chemical structures and controlled degradation through hydrolysis, allowing tunability of mechanical strength and degradation rates, synthetic polymers are commonly addressed for clinical applications, easing translation to medical devices. However, synthetic polymers can have lower bioactivity than natural polymers, potentially requiring surface modifications or incorporation of biological cues to enhance cell attachment and function, and eventually cause local inflammation due to the acidic degradation products [Ba, 2014].

For bone healing applications, bioceramic scaffolds, such as hydroxyapatite (HA) and tri-calcium phosphate (TCP), have been widely used [OB, 2011]. Bioceramic scaffolds are known for their high mechanical stiffness (high Young's modulus, ranging from 57Mpa to over 300MPa), and hard, brittle surfaces. However, some bioceramics such as alumina and zirconia can reach to 200 - 300 GPa (much higher than that of bone), and therefore, they are never implanted in close contact with the bone to prevent stress shielding [Wa, 2025].Their strong biocompatibility, attributed to the chemical and structure similar to that of native bone minerals, makes them particularly suitable for bone-related applications. Ceramics support bone regeneration by promoting osteoblast proliferation and differentiation. As a result, they have been widely used in orthopedic and dental surgeries, both as fillers for bone defects and as coatings for metallic implants to enhance integration with surrounding bone tissue [OB, 2011]. However, their use in broader tissue engineering applications is constrained by certain drawbacks, such as their brittleness, limited moldability for complex shapes, and the inability of new bone tissue formed within porous HA scaffolds to endure the mechanical stresses required for normal bone remodeling [Va, 2023]. Bioactive glasses_are highly promising materials among bioceramics used in tissue engineering, especially for bone regeneration. It chemically bonds with both hard and soft tissues and releases therapeutic ions like calcium and silicon that stimulate cell proliferation and tissue healing [Da, 2023]. Bioactive glass can be classified into three main types: silicate-based, borate-based, and phosphate-based glasses. Silicate and borate glasses degrade incongruently, often precipitating HA on their surfaces, whereas phosphate glasses exhibit congruent degradation, dissolving layer by layer [Ka, 2023]. Some compositions of bioactive glasses also have inherent antibacterial properties, helping to reduce infection risks. Although inherently brittle, some of them can be processed into porous scaffolds that support vascularization and can be strengthened by forming glass-ceramics or combined with polymers for enhanced mechanical properties [Ca, 2021]. These multifunctional capabilities make bioactive glass a standout candidate for regenerative medicine applications. In this thesis, 1393B20 glass having composition $43.68SiO_2$-$10.92B_2O_3$-$1.7P_2O_5$-$6Na_2O$-$7.9K_2O$-22.1CaO-7.7MgO in mol% is used as a bioactive glass for fabricating the 3D printed scaffold. This bioactive glass is a specialized borosilicate bioactive glass used in bone tissue engineering, particularly for fabricating 3D printed scaffolds Thanks to its scaffold mechanical properties, rapid HA formation, excellently compatible to cell, and enhanced dissolution and bioactivity, 1393B20 is promising for clinical translation in bone defect repair and potentially other tissue engineering fields [Sz, 2024].

2.1.3 Fabrication methods

Scaffold fabrication involves various techniques aimed at creating 3D porous structures that support cell attachment, growth, and tissue regeneration. These methods are chosen based on the required scaffold properties like porosity, mechanical strength, biodegradability, and biological response [Ku, 2022]

Conventional methods include solvent casting and particulate leaching, freeze-drying, gas foaming, electrospinning, and thermally induced phase separation, each offering various degrees of porosity control, mechanical strength, and suitability for different ma-

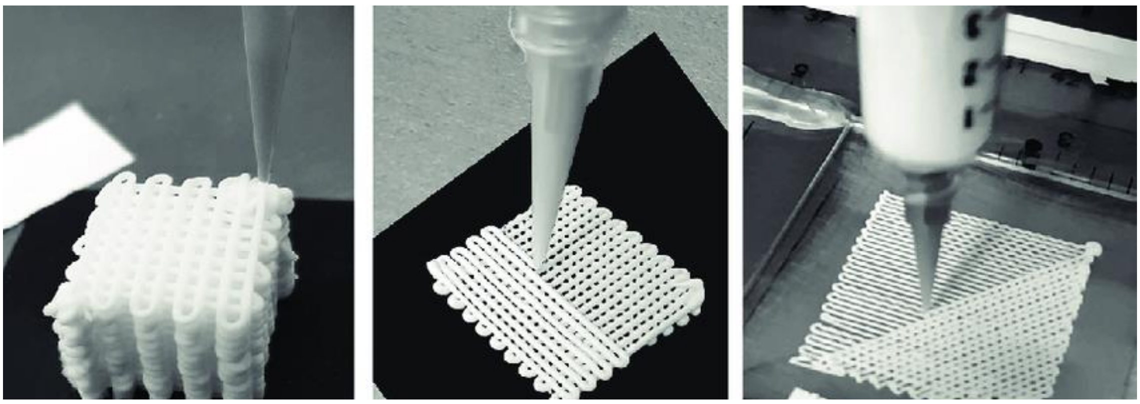

Figure 2: 3D printed scaffolds using three types of nozzles: (a) 0.8 mm; (b) 0.6 mm; and (c) 0.4 mm [Pr, 2020]

terials but sometimes involving toxic solvents or limited precision. Advanced and emerging techniques like 3D printing (including fused deposition modeling, stereolithography, and selective laser sintering) and bioprinting allow precise control over scaffold geometry, pore size, and the incorporation of cells during fabrication, enabling customizable, biomimetic scaffolds that better replicate native tissue architecture (Figure 2). Hybrid approaches combining these methods are also being explored to optimize macro- and microporosity for specific applications. The choice of fabrication method balances factors such as material biocompatibility, scaffold properties, manufacturing complexity, and tissue-specific requirements [Ku, 22] [Ve, 22] [Col, 21] [Bh, 22].

In this research, Direct Ink Writing (DIW), also known as robocasting, was carried out. This is an extrusion-based additive manufacturing (AM) technique especially widespread for making ceramic and bioactive glass scaffolds. In this method, a computer-controlled nozzle deposits a paste-like, highly concentrated ceramic ink layer by layer according to a previously optimized script [La, 2022].

2.2 Applications and main issues with scaffolds

Scaffolds are widely used in tissue engineering and regenerative medicine to provide a temporary three-dimensional structure that supports cell attachment, proliferation, and differentiation, ultimately guiding new tissue formation. Their applications span bone regeneration for critical-size defects, cartilage repair in joint injuries, skin substitutes for burns and chronic wounds, nerve regeneration via guidance conduits, vascular grafts for engineered blood vessels, dental regeneration for alveolar bone and periodontal tissue, and controlled drug delivery through incorporation of therapeutic agents. Beyond clinical uses, scaffolds also serve as in vitro models for disease research and drug screening, enabling physiologically relevant cell–tissue interactions under laboratory conditions. By tailoring scaffold materials, architecture, and degradation rates, they can be optimized for both structural and biological requirements across diverse biomedical applications [OB, 2011], [Bo, 2012].

However, the use of scaffolds in tissue engineering and bone repair can have a notable risk of infection. This infection risk can seriously complicate outcomes and increase patient morbidity, healthcare costs, and the likelihood of further interventions such as implant removal or repeat surgeries [CT, 2014]. Moreover, bacteria can adhere to the surface of the implant and form biofilms, structured communities of bacteria that are resistant to immune responses and antibiotics. As the presence of a scaffold can introduce a new surface for both host cells and bacteria to colonize—particularly in complex tissue environments or bone defects [Qi, 2024]—the outcome of this competition is crucial in determining the overall success of the implant.

2.2.1 Infection eradication

Several methods have been carried out to prevent infections ranging from antibiotics, proper hygiene practices by healthcare professionals, environmental control such as patient isolation or negative pressure rooms, surface modifications and coatings, sterilization methods, and strict adherence to sterile procedures during medical interventions [CT, 2014]. Among these solutions, engineered biomaterials or scaffolds used to locally control infection is rapidly expanding. Especially, infection eradication in implantation, particularly in tissue-engineered scaffolds, relies on preventing bacterial colonization (antimicrofouling surfaces) and biofilm formation, and ensuring rapid immune or antimicrobial responses to control pathogens at the implant site. Specifically, effective infection eradication around scaffolds in implantation integrates prevention of bacterial adhesion, localized antimicrobial activity, immune modulation, and sterilization, with ongoing research focused on multifunctional, responsive scaffolds that control infections while promoting tissue regeneration [Wu, 2025].

2.2.2 Nitric oxide for infection eradication

Nitric oxide (NO) is naturally secreted by human cells and, among other functions, plays a significant role in infection eradication due to its powerful antimicrobial properties [Lu, 2022]. It is an endogenous molecule produced by immune cells that, at high concentrations, kills pathogens by causing nitrosative and oxidative damage to DNA, proteins, and lipids of bacteria, fungi, and viruses [Sc, 2012]. NO disrupts microbial metabolism, inhibits growth, and can lead to death of the bacteria by mechanisms including DNA deamination, protein nitrosylation, and lipid peroxidation. Importantly, NO's broad antimicrobial activity targets a wide range of pathogens with minimal risk of resistance development. Due to these effects, various NO delivery systems are being developed for localized antimicrobial therapy, including NO-releasing scaffolds that provide sustained release to infected sites, promoting bacterial clearance while supporting tissue regeneration [Si, 2020]. NO can also disrupt biofilms, which are typically resistant to antibiotics, enhancing infection eradication in implant-related infections. Thus, NO's dual role as an immune signaling molecule and a direct antimicrobial agent makes it a promising agent for infection control in biomedical implants and tissue engineering scaffolds. Therefore, improving the secretion of NO using light is a promising and advanced approach in biomedical implantation.

2.2.3 Scaffold emitting green light to release NO

Light-triggered release of NO involves the use of specially designed molecules called NO photodonors that release NO upon exposure to specific wavelengths of light. This approach allows precise spatial and temporal control over NO delivery, which is critical because NO's biological effects depend heavily on its concentration and localization [DD, 2008]. NO photodonors remain stable until irradiated with light of a particular wavelength (e.g., UV, blue, green, red, or near infrared). Upon light exposure, these compounds undergo photochemical reactions that break bonds and liberate NO [Zh, 2020].

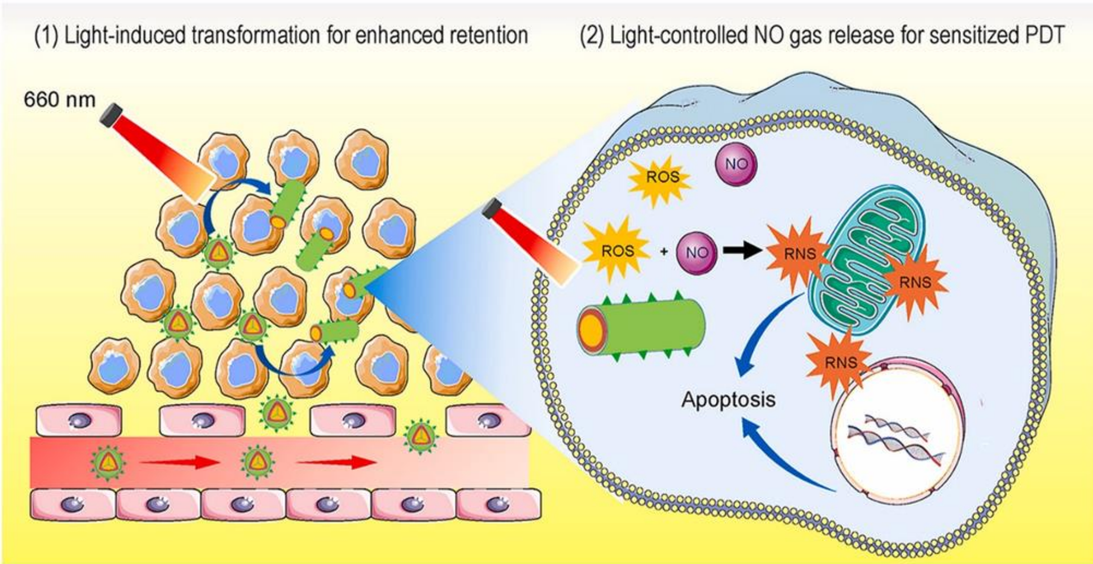

Figure 3: Schematic illustration of the light-triggered NO generation and structural transformation of peptide-based NPs for enhanced intratumoral retention and sensitizing PDT [Li, 2022].

Green light can induce the release and modulation of nitric oxide (NO) in biological tissues through photochemical processes involving photolabile NO donor compounds, such as S-nitrosothiols (RSNOs), dinitrosyl iron complexes (DNICs), and S-Nitroso-N-Acetylpenicillamine (SNAP). Specifically, green light (around 540–545 nm) triggers the weakening or reorganization of chemical bonds within these NO donors in case of SNAP, enabling the transfer or release of NO locally without necessarily releasing it completely into the surrounding environment [Gh, 2024].

2.3 $SrAl_2O_4:Eu^{2+}$, Dy^{3+} phosphors with green afterglow

Persistent luminescence particles, also known as afterglow phosphors or persistent luminescence nanoparticles (PeLs), are a class of materials that continue to emit light long after the excitation source is removed [Ab, 2016]. These materials store energy from an external light source (UV, visible, NIR, X-ray) and release it slowly as visible light over time. The materials involve energy traps (defects or dopants) that capture electrons or holes (space without electrons) during excitation, and trapped charges are gradually released, producing sustained luminescence. $SrAl_2O_4$-based phosphors are valued for their high brightness, chemical stability, and long emission duration, making them useful in emergency signage, bioimaging, and security markings. However, a key limitation for their biomedical applications is that they must be charged with UV light, and UV radiation cannot penetrate human skin effectively, restricting their use for *in vivo* deep-tissue application without alternative excitation strategies [Me, 2008].

2.3.1 Green afterglow after NIR charging

Upconversion (UC) luminescence is a nonlinear optical process in which low-energy photons in the near-infrared (NIR) region are sequentially absorbed and converted into higher-energy visible emissions. In Yb^{3+}/Tm^{3+}-doped crystals, Yb^{3+} acts as an efficient sensitizer due to its strong absorption around 975–980 nm and its ability to transfer energy to Tm^{3+} activator ions, which subsequently emit in the blue and near-UV regions through multiple excited-state transitions. When the blue emission is sufficiently intense, it can optically excite a phosphor, producing a persistent green afterglow even after NIR excitation ceases.

The blue emission under 980nm pumping is due to:

- Yb^{3+} (Ytterbium) typically acts as a sensitizer because it has a large absorption cross-section around 975 nm or 980 nm in the NIR region. It efficiently absorbs infrared light and transfers the absorbed energy to activator ions like Tm^{3+}. Yb^{3+} has a simple energy level structure with mainly two levels, which helps in efficient energy transfer. Because Yb^{3+} can be doped at high concentrations without much self-quenching, it acts as an effective energy harvester to boost upconversion [Gu, 2014].

- Tm^{3+} (Thulium) is the activator ion that emits photons after receiving energy from Yb^{3+}. It has multiple excited states enabling it to emit visible blue and near-UV wavelengths via sequential energy transfers and excited state absorption.

The balance of Yb^{3+} and Tm^{3+} dopant concentrations is crucial to reduce cross-relaxation and self-quenching, which would lower upconversion efficiency [Ba, 2018].

If the intensity of the blue emission is strong enough, then it can be used to charge the PeL phosphor, as shown in Figure 4.

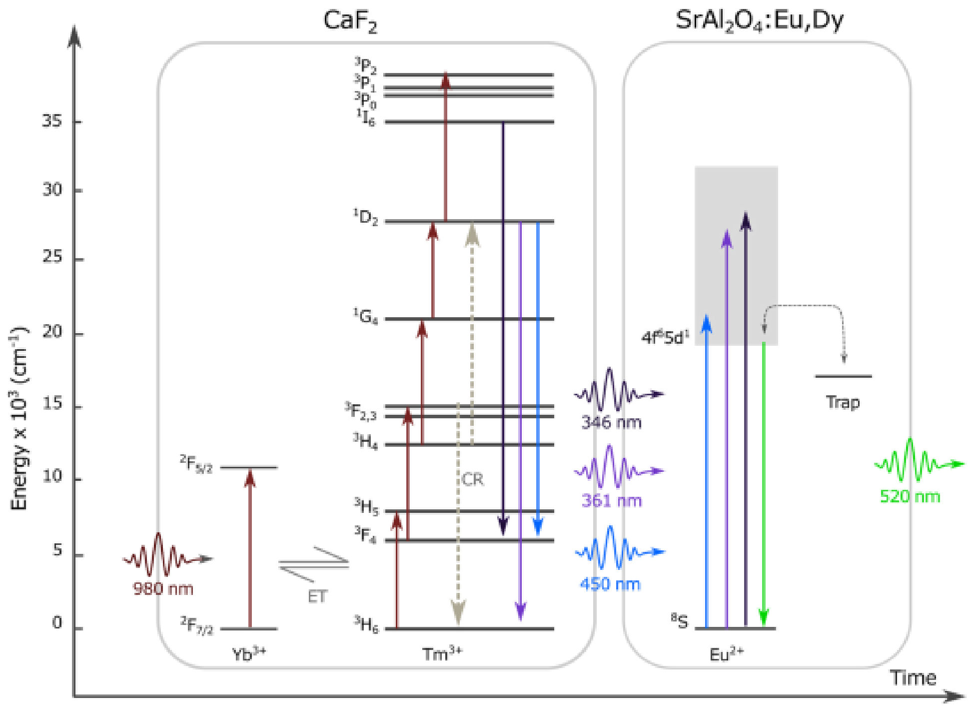

Figure 4: Schematic representation of the different luminescence processes that lead to the emission of green afterglow after the exposure of the composite to 980 nm infrared light. [Ar, 2022]

However, the 980nm wavelength is readily absorbed by water, which will cause warming/heating [Ah, 2010]. Thus, excitation at 808 nm is preferred as it is much less absorbed by water. The blue emission under 808 nm pumping follows the energy transfer mechanism as shown in Figure 5. Such upconversion process can be obtained from materials with low phonon energy as the low phonon energy of the host decreases the rate of nonradiative multiphonon relaxation from upper levels leading to high efficiency of the up-conversion process. Phosphate bioactive glass are known to have high phonon energy which quenches the UC fluorescence due to multi-phonon transitions that shorten the lifetimes of metastable states [Ar 2022]. Hence, UC crystals with low phonon energy can be added in the borosilicate bioactive glass in order to prepare a scaffold which emits efficient blue light under NIR charging [Gh, 2024].

These crystals can be prepared using different techniques such as flux-growth, hydro-

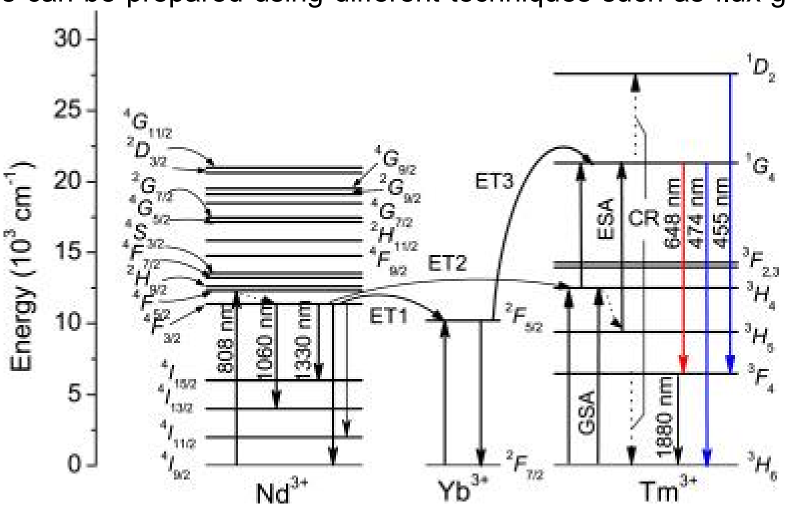

Figure 5: Energy level diagrams of Tm3+, Yb3+, Nd3+ ions and the possible UC luminescence processes of Tm3+ under 808 nm excitation [Ti, 2020].

thermal and sol-gel method. In this study, the crystals were synthesized using solid-state reaction where solid precursor materials are intimately mixed and then heated at high temperatures to induce chemical reactions that form the desired luminescent compound. First, solid raw materials (e.g., oxides, carbonates, nitrates) are homogeneously mixed in stoichiometric proportions. Then, the mixture is heated at high and controlled temperature to promote diffusion and reaction between the solids without melting. Finally, formation of crystalline luminescent materials occurs through solid-state diffusion and rearrangement of atoms in the solid phase. Solid-state reactions are widely used for preparing phosphors and luminescent materials because they are relatively simple, scalable, and yield highly crystalline products with good thermal stability [Qi, 2015]. However, the method usually requires long heating times and high temperatures (often >800°C) to achieve complete reaction and homogeneity.

This research focused on $NaNbO_3$ (sodium niobate), a perovskite-structured oxide known for its antiferroelectric behavior, photocatalytic activity, and as a host material for upconversion luminescence. When doped with rare-earth ions such as Tm^{3+} and Yb^{3+}, $NaNbO_3$ nanocrystals exhibit significant upconversion properties, converting near-infrared (NIR, typically 976–980 nm) excitation into visible emission [Xi, 2016]. Moreover, $NaNbO_3$ nanocrystals allow for nanostructuring and straightforward rare-earth doping during synthesis, supporting efficient upconversion and luminescent applications. In addition, the research also considers $CaTeO_3$ (calcium tellurate), a tellurate perovskite oxide that has recently been explored as a host for upconversion luminescence, typically by doping with rare-earth ions such as Nd^{3+}, Yb^{3+}, and Tm^{3+}. This crystal synthesis parameters for luminesence application have been optimized based on Ye et al [Ye, 2020].

In this context, the goal of this study is to prepare a scaffold able to emit long lasting green emission after NIR charging.

3. EXPERIMENTAL

3.1 Scaffold fabrication

The scaffold fabrication process involved synthesizing and combining functional materials to create bioactive, luminescent, and mechanically stable constructs suitable for advanced applications [Fu, 2011]. This section outlines the preparation of the glass matrix, the synthesis of the upconverter crystals, and printing of the final scaffold.

3.1.1 Glass melting

Borosilicate bioactive glass with the $43.68SiO_2$–$10.92B_2O_3$–$22.10CaO$–$7.90K_2O$–$6.00Na_2O$–$1.70P_2O_5$–$7.70MgO$ mol% composition (labeled as 1393B20) was synthesized using analytical-grade Na_2CO_3 (Thermal Scientific,99.95%), $NH_4H_2PO_4$ (Sigma-Aldrich,98%), $CaCO_3$ (Alfa Aesar,99.5%), MgO (Aldrich,99%), H_3BO_3 (Sigma- Aldrich,99.5%), K_2CO_3 (Sigma,99%), and SiO_2 (Merk 99.9%) [Sz, 2024]. The composition was melted in 60 g batches using a platinum crucible. The precursors were heated up at 800 °C with a rate of 16 °C/min, kept at this temperature for 15 minutes, and successively heated up to 1450 °C with a rate of 13 °C/min. The melt was finally kept at 1450 °C for 30 minutes. The melting process was set in air using an LHT 02/17 LB Speed electric furnace (Nabertherm GmbH, Lilienthal, Germany). The molten glass was then cast into a graphite mold and annealed in a Nabertherm L 3/12 electric muffle furnace. Annealing was carried out at 500 °C for 8 hours.

After annealing, the casted glasses were crushed and milled in a planetary ball mill (Fritsch GmbH, Idar-Oberstein, Germany), and then sieved (Gilson Company, Inc., Ohio, USA) to a particle size of less than 38 µm.

3.1.2 Upconverter crystal synthesis

$CaTeO_3$ tri-doped Nd^{3+}/Yb^{3+}/Tm^{3+} crystals was synthesized as in [Ye, 2020]. The composition (in at%) was 44.07 CaO, 51.98 TeO_2, 0.21 Tm_2O_3, 1.04 Yb_2O_3, 0.73 Nd_2O_3. First, the batch was heated from room temperature up to 600°C at a 3°C /min and kept the temperature for 3 hours. After cooling down to room temperature, the sample was grinded to be heated up to 800°C at a 3°C/min and the temperature was maintained for other 3 hours.

$NaNbO_3$ tri-doped $Nd^{3+}/Yb^{3+}/Tm^{3+}$ crystals was synthesized based on parameters used in [Xi, 2016], which used Er^{3+} and Yb^{3+}. Crystals were prepared with different RE dopants: Yb_2O_3, Nd_2O_3, and Tm_2O_3 contents in order to determine the best ratio for intense blue upconversion under NIR pumping. The precursors to synthesize the crystals were Na_2CO_3 and Nb_2O_5 (Thermo Fisher Scientific, ≥ 99.5% purity). The batches in quartz crucible were heated at different temperature for different time, depending on the contents of RE dopnats, with the heating rate of 3°C/min.

Table 2 summarizes the RE dopant concentration and heat treatment conditions used for crystals preparation.

Table 2: Crystals $NaNbO_3$ and $CaTeO_3$ doped RE content and heat treatment

Crystals	RE dopants (at%)			Heat treatment
	Yb	Tm	Nd	
$NaNbO_3$	0.5	0.25	0	RT (Room Temperature) => 400°C (2h) => 600°C (2h) => 900°C (2h) 3°C/min
	1	0.25	0	
	1.5	0.25	0	
	5	0.25	0	RT => 700°C (4h) => RT => 1200°C (4h) 3°C/min
	10	0.25	0	
	15	0.25	0	
	20	0.25	0	
$CaTeO_3$	1	0.2	0.7	RT => 600°C (3h) => RT (crush) RT => 800°C (3h) => RT (crush) 3°C / min

3.1.3 3D printing

To prepare the ink for 3D printing, an aqueous solution of Pluronic® F-127 (Sigma-Aldrich, USA) was employed as a sacrificial binder. The solution was obtained by mixing and stirring Pluronic® in ultrapure water (30 % wt/wt) for ~8 h in an ice bath, to maintain the aimed low viscosity of the polymer at low temperature [Ku, 2004].

1393B20 glass was mixed with the UC crystals and the commercial (PeL) phosphors (Realglow®), up to 15 wt% as in Nguyen et al 2022 [Ng, 2022]. For each crystal and excitation wavelength, different ratios between the UC and PeL crystals up to 15 wt% as shown in Table 3 in order to determine the optimized ratio to obtain visible green afterglow after NIR charging.

Table 3: Different ratios of UC crystals and PeLs for strongest green afterglow effect.

1393B20 glass (wt%)	Crystals	UC crystals and PeL (15 wt%)	
		UC crystals wt%	PeL wt%
85	$Ca_{(1-x-y-z)}Yb_xTm_yNd_zTeO_3$ (where x=1, y=0.2 and z= 0.7 in at%).	12.5	2.5
		10	5
		7.5	7.5
		5	10
		2.5	12.5
	$Na_{(1-x-y)}Yb_xTm_yNbO_3$ (where x=15 and y=0.25 at%)	12.5	2.5
		10	5
		7.5	7.5
		5	10
		2.5	12.5

The resulting composite is mixed by vortexing at 2500 RPM for approximately 30 seconds, followed by cooling in an ice bath for another 30 seconds five times. Although some bubble formation is inevitable during vortexing, it should be minimized, and any bubbles that do form are expected to be invisible.

The obtained ink was carefully loaded into a syringe, which was then connected to the dispensing cartridge of the 3Dn-Tabletop printer (nScrypt Inc., Orlando, Florida, USA). The loaded cartridge was left 30 min at room temperature to allow the ink to set. After that, it was attached onto the printer's dispensing module, ensuring proper alignment for controlled extrusion. A 0.4 mm tip (Nordson EFD Optimum® SmoothFlow™, Westlake, Ohio, USA) was attached to the cartridge.

The 3D printer operates based on a predefined digital script (txt format), which was uploaded into the system through the Machine Tool 3.0 system software. This script determines the layer-by-layer printing path, and, through the program, it was possible to set the speed and the pressure for the extrusion, both dispensing parameters being tailored for the rheological properties of the ink. The 3D scaffold was accordingly printed onto an acrylic sheet (Folex AG, Seewen, Switzerland). A continuous flow was maintained by setting and adjusting the pressure in the range of 15.0–25.0 psi.

The printed scaffolds were then left to dry in a ventilated oven at 37°C overnight. This drying step is essential to remove any residual moisture, solidify the structure, and minimize the shrinkage occurring during the sintering step [Va, 2017]. After being dried, the scaffolds were sintered at 625°C (heating rate: 10°C/min) for 1 hour. This process ensured the fusion of powder particles together to form a solid, porous structure suitable for tissue engineering applications, in parallel with the elimination of the sacrificial binder [Sz, 2024].

3.2 Characterization

3.2.1 Spectroscopic properties

The afterglow properties of the mixture containing the UC crystals combined with the PeL phosphors were examined in the dark at room temperature after charging for 10 min at 808 and 980nm. Laser excitation was generated by a Thorlabs ITC4001 laser diode/temperature controller (Thorlabs, Inc., USA), operating at a current of 1A. Initially, the samples were irradiated with the laser for 10 minutes, during which the UC crystals absorbed the laser energy and upconverted it to recharge the previously discharged PeL. After turning off the laser, the afterglow from the samples was evaluated. Videos were recorded in order to compare the intensity of the green afterglow.

The UC emissions spectra of the crystals were measured by Spectro 320 optical spectrum analyzer (Instrument Systems Optische Messtechnik GmbH, Germany). Using the same excitation source as above, at 808 and 980nm, the measurement was conducted at room temperature and crushed powders were used to observe the difference of UC intensity.

3.2.2 X-ray diffraction (XRD)

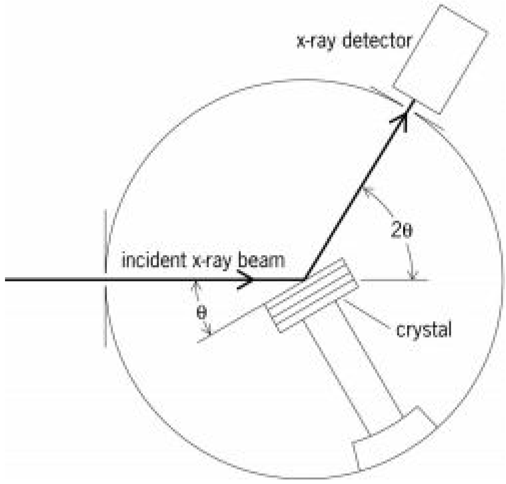

Figure 6: Schematic of XRD experiment. [x-ray diffraction, 2002]

The PANalytical EMPYREAN multipurpose X-ray diffractometer (PANalytical Almelo, The Netherlands) was used to measure the XRD patterns of the crystal and scaffolds. The diffractograms were measured from $2\theta = 10°$ to $80°$ with a step size of 0.026° using Ni-filtered Cu-Kα radiation.

XRD relies on the diffraction of X-rays as they interact with the crystal lattice of a material. When a beam of X-rays strikes a crystal, the rays are scattered by the atoms in the lattice. For certain specific angles, the scattered rays interfere constructively, producing a pattern unique to the atomic arrangement of that material [Ji, 2018]. This relationship is defined by Bragg's Law:

$$n\lambda = 2dsin\theta \qquad (1)$$

where λ is the X-ray wavelength, d is the spacing between crystal planes, and θ is the diffraction angle. By analyzing the angles and intensities of these peaks, XRD provides information about the crystal structure, phase composition, and interplanar spacing of the material.

4. RESULTS AND DISCUSSION

The goal of this study was to develop 3D printed porous biophotonic scaffolds with long lasting green emission after NIR charging.

4.1 Development of crystals with blue emission under NIR pumping

Long lasting green emission after NIR charging is achieved by adding, in the scaffolds, crystals which emit blue light under NIR pumping and the $SrAl_2O_4$:Eu^{2+},Dy^{3+} phosphors with green persistent luminescence (PeL) after UV charging as in [Ar, 2022]. The intensity of the blue emission needs to be strong enough to charge the PeL phosphors.

In this study, blue emission under NIR pumping is obtained using Tm^{3+}, Yb^{3+} and/or Nd^{3+} as dopants. As explained in the background chapter (§2.2.2.2), the NIR is absorbed by Nd^{3+}/Yb^{3+} and transferred to Tm^{3+} from which the blue emission is obtained. This upconversion process is obtained if the rare-earth ions are located in host with low phonon energy. In this work, the study focused on two crystals: $CaTeO_3$ and $NaNbO_3$.

As in [Ye, 2020], crystals with the composition $Ca_{(1-x-y-z)}Yb_xTm_yNd_zTeO_3$ (where x=1, y=0.2 and z= 0.7 in at%) was synthesized using the solid-state reaction. The XRD pattern of the fabricated crystals, shown in Figure 7, matches well with the theoretical $CaTeO_3$ reference card (ICDD 04-016-8121), indicating successful incorporation of RE dopants into the crystal lattice.

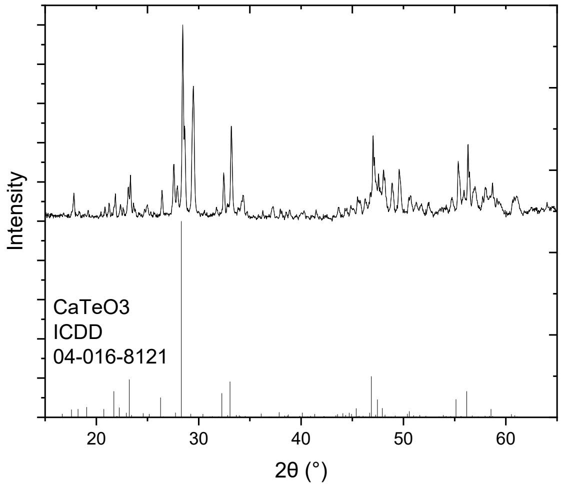

Figure 7: XRD pattern of crystal the $Ca_{(1-x-y-z)}Yb_xTm_yNd_zTeO_3$ (where x=1, y=0.2 and z= 0.7 in at%).

$Na_{(1-x-y)}Yb_xTm_yNbO_3$ (where x=5-20, and y=0.25 at%) crystals were also synthesized via solid-state reaction using the work by [Ch, 2010]. However, there is no study on tri-doped $NaNbO_3$ crystals. Their XRD patterns are presented in Figures 8a.

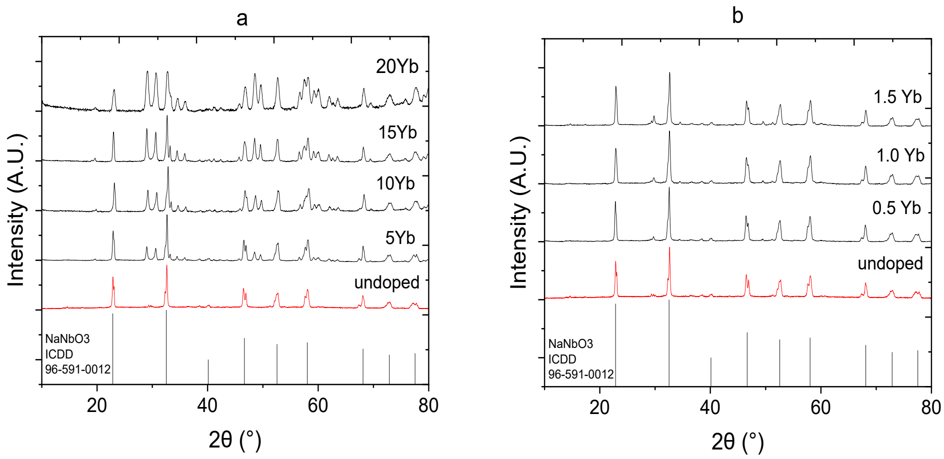

Figure 8: XRD pattern of $Na_{(1-x-y)}Yb_xTm_yNbO_3$ (where x=5-20 and y=0.25 at%) crystals (a) and $Na_{(1-x-y)}Yb_xTm_yNbO_3$ (where x=0.5-1.5 and y=0.25 at%) crystals (b)

In addition to the XRD peaks expected for the $NaNbO_3$ crystal, several unexpected peaks appeared depending on the rare-earth content (Figure 8a). As Yb^{3+} concentration increased, the number and intensity of these unwanted peaks rose, suggesting incomplete incorporation of Yb^{3+} into the crystal structure. This is especially evident in the sample prepared with 20 at% Yb^{3+}. To minimize these undesired phases, three additional $Na_{(1-x-y)}Yb_xTm_yNbO_3$ (where x=0.5-1.5, and y=0.25 at%) crystals were prepared with lower Yb^{3+}

concentrations (0.5 to 1.5 at%) while maintaining Tm^{3+} at 0.25 at%. These samples underwent a multi-step heating process: ramping from room temperature to 400°C (held for 2 hours), then to 600°C (held for 2 hours), and finally to 900°C (held for 2 hours) [Te, 2023]. The XRD pattern of these samples in Figure 8b showed fewer unexpected phases and better alignment with the $NaNbO_3$ reference, suggesting more complete dopant incorporation when using lower amount of Yb^{3+}. However, it was not possible to prepare pure $NaNbO_3$ single phase crystal despite doping the crystals with low amount of rare-earth ions.

The UC spectra of the $Ca_{(1-x-y-z)}Yb_xTm_yNd_zTeO_3$ (where x=1, y=0.2 and z= 0.7 in at%) crystal were measured using 808 and 980nm pumping. The crystal is the only crystal with blue UC under both 980 nm and 808 nm excitation which is consistent with [Ye, 2020]. The upconversion emission spectra upon both excitation is shown in Figure 9:

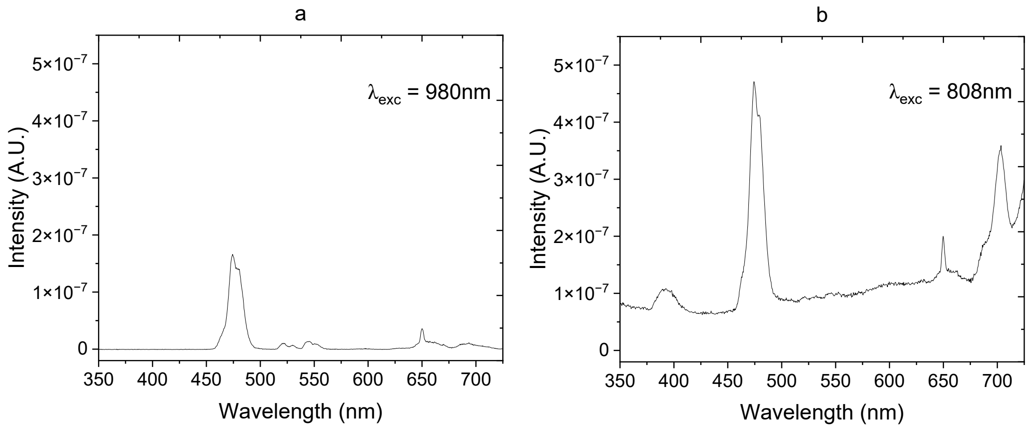

Figure 9: Upconversion spectrum of $Ca_{(1-x-y-z)}Yb_xTm_yNd_zTeO_3$ (where x=1, y=0.2 and z= 0.7 in at%) crystal under a) 980 nm and b) 808 nm excitation

The UC spectra exhibit emission bands at 476 nm and at 650 nm which are due to $^1G_4$-$^3H_6$ and $^1G_4$-$^3F_4$ transition of Tm^{3+}, respectively [Ye, 2020]. One should mention that the intensity of the blue emission is small upon 980 nm excitation compared to 808nm excitation . The increase of UC intensity in these wavelength upon 808nm excitation can be attributed due to the absorption Nd $^{3+}$ ions at these wavelength and subsequent energy transfer to Yb^{3+} and then to Tm^{3+}.

Blue emission was observed from the $Na_{(1-x-y)}Yb_xTm_yNbO_3$ (where x=5-20 and y=0.25 at%) crystals only when using 980 nm pumping. The normalized upconversion spectra of these crystals are presented in Figure 10a. They exhibit the same emission bands related to the 4f-4f transitions of Tm^{3+} than in Figures 9. Although these crystals with lower-Yb^{3+}content (<5at%) showed single phase of $NaNbO_3$ upon XRD (Figure 9b), their blue upconversion intensity was too weak. Conversely, samples with higher Yb^{3+} concentrations (5–20 at%) exhibited stronger blue upconversion.

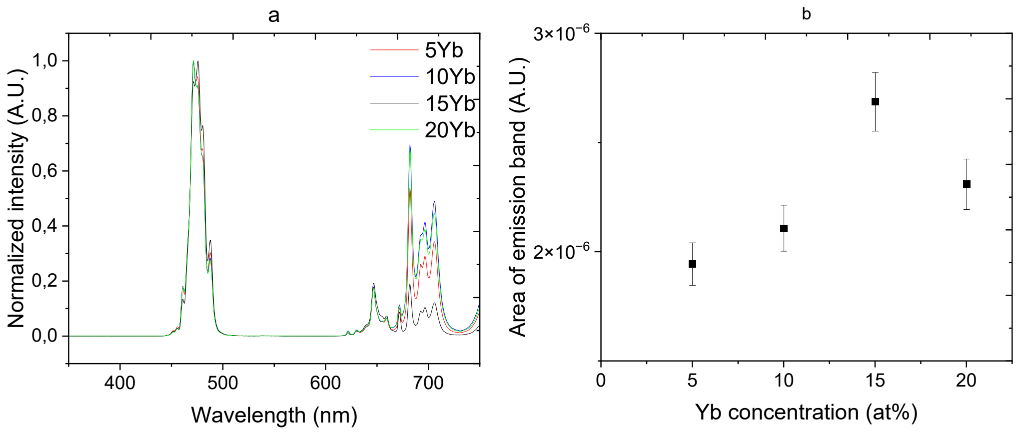

Figure 10: Normalized emission spectra of the $Na_{(1-x-y)}Yb_xTm_yNbO_3$ (where x=5-20 and y=0.25 at%) crystals (a) and intensity of the emission at 475 nm as a function of Yb^{3+} concentration (b). The spectra are obtained using 980 nm excitation.

From the upconversion spectra presented in figure 10, it is evident that an increase in Yb^{3+} content to 15 at% leads to an increase in the intensity of the blue emission. However, due to concentration quenching [Ar, 2022], the intensity of the blue emission decreases when the concentration of Yb^{3+} beyond 15 at%.

Therefore, crystals with composition $Na_{(1-x-y)}Yb_xTm_yNbO_3$ (where x=15 and y=0.25 at%) which had the highest blue emission upon 980nm was chosen for scaffold synthesis along with crystals with composition $Ca_{(1-x-y-z)}Yb_xTm_yNd_zTeO_3$ (where x=1, y=0.2 and z= 0.7 in at%) which had blue emission upon both 980nm and 808nm excitation...

4.2 3D printed Scaffold

First step was to check if the blue emission from the crystals was strong enough to charge the PeL phosphors. As explained in [Ng, 2022], the amount of crystals in scaffolds should not exceed 10-15 wt% in order to maintain the required mechanical properties of the scaffolds. Larger concentration of dopants leads to fragile scaffold. Samples were then prepared with up to 15 wt% of PeL and UC crystals (2.5-12.5; 5-10; 7.5-7.5; 10-5 and 12.5-2.5). They were charged with 980 nm for 10 min. The following three samples showed visible green afterglow after 980 nm excitation:

- 5 wt% PeL / 10 wt% $CaTeO_3$

- 7.5 wt% PeL / 7.5 wt% $NaNbO_3$

- 10 wt% PeL / 5 wt% $NaNbO_3$

These PeL/UC mixtures were then combined with 1393B20 glass and suspended, as described in §3.1.3, into the Pluronic® solution, to prepare the ink. Only the control ink, consisting in the glass without addition of PeL/UC crystals, was successfully printed (Figure 10).

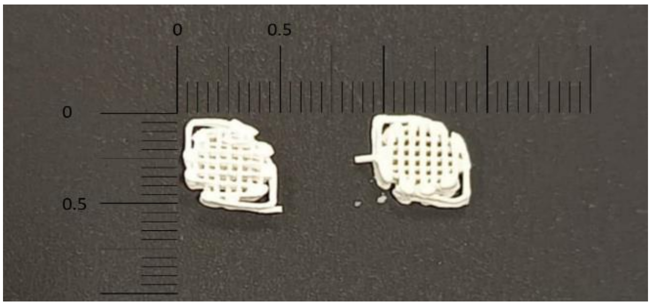

Figure 11: 3D printed undoped scaffolds.

It was not possible to extrude the doped ink through the nozzle likely due to the presence of the upconverter crystals which have large size and large size distribution, which possibly occlude blocking the tip. It is possible that the glass particles, prepared more than 2 months earlier, may have been hydrated, despite the adequate storage in a desiccator, because of the high surface-to-volume ratio, potentially causing the start of a degradation process. This phenomenon could have led to the failure in chemically embedding the dispersed phase (PeL/UC crystals) into the glass matrix, negatively affecting the ink printability. Because of this, the inks that could have not been printed were manually extracted from syringes for sintering and characterization. For each cartridge, half of the extracted volume was sintered at 625°C for 1 hours using approximately 10°C/min as in [Sz, 2024], and half was left unsintered. The XRD pattern of the sintered inks exhibit peaks which can be assigned essentially to the UC crystals and PeL phosphors, confirming their successful integration into the glass matrix (Figure 12). No crystallization of occured during the sintering process which was confirmed from the XRD.

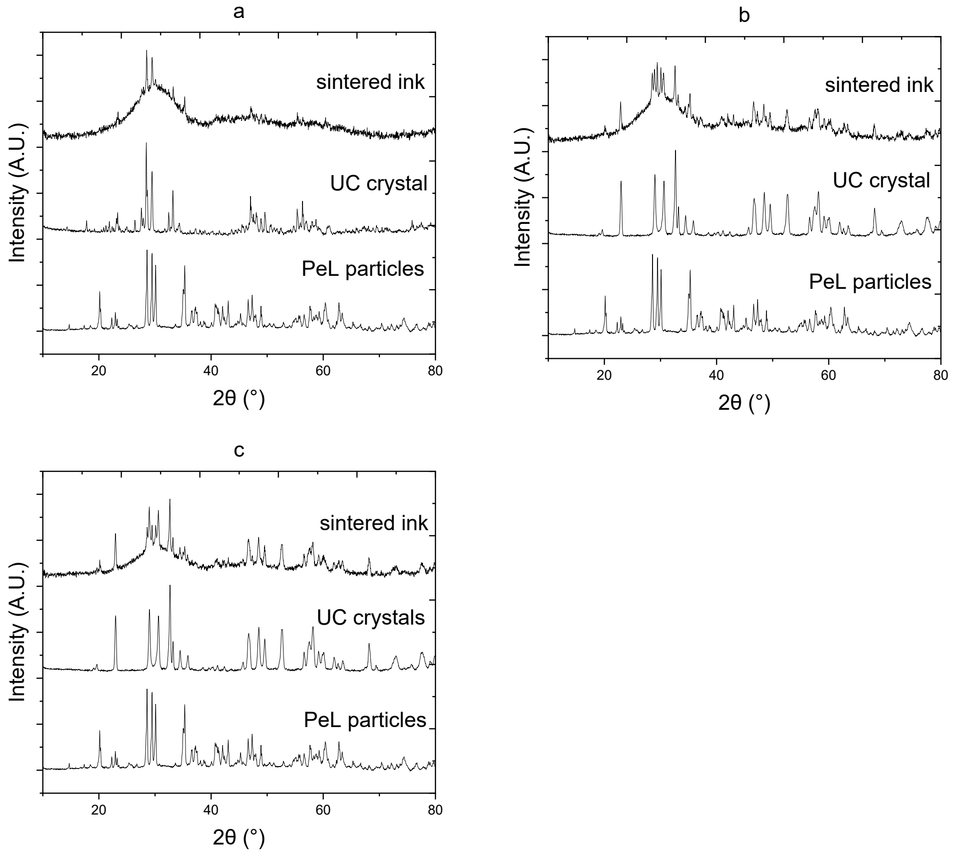

Figure 12: XRD pattern of 3D printing ink sintered with 10 wt% $Ca_{(1-x-y-z)}Yb_xTm_yNd_zTeO_3$ (where x=1, y=0.2 and z= 0.7 in at%) (a), 7.5 wt% $Na_{(1-x-y)}Yb_xTm_yNbO_3$ (where x=15 and y=0.25 at%) (b) and 5 wt% (c) $Na_{(1-x-y)}Yb_xTm_yNbO_3$ (where x=15 and y=0.25 at%).

The picture of the inks prior to and after sintering in daylight and after stopping UV charging are shown in Figure 13. Homogeneous green afterglow can be observed from the inks after being charged for 1 min with UV lamp confirming that the PeL phosphors do not degrade when preparing the ink and they are well dispersed in the inks. A slight decrease in intensity of the green afterglow is observed after sintering and can be related to the creation of defects in the phosphors as mentioned in [Oj, 2018].

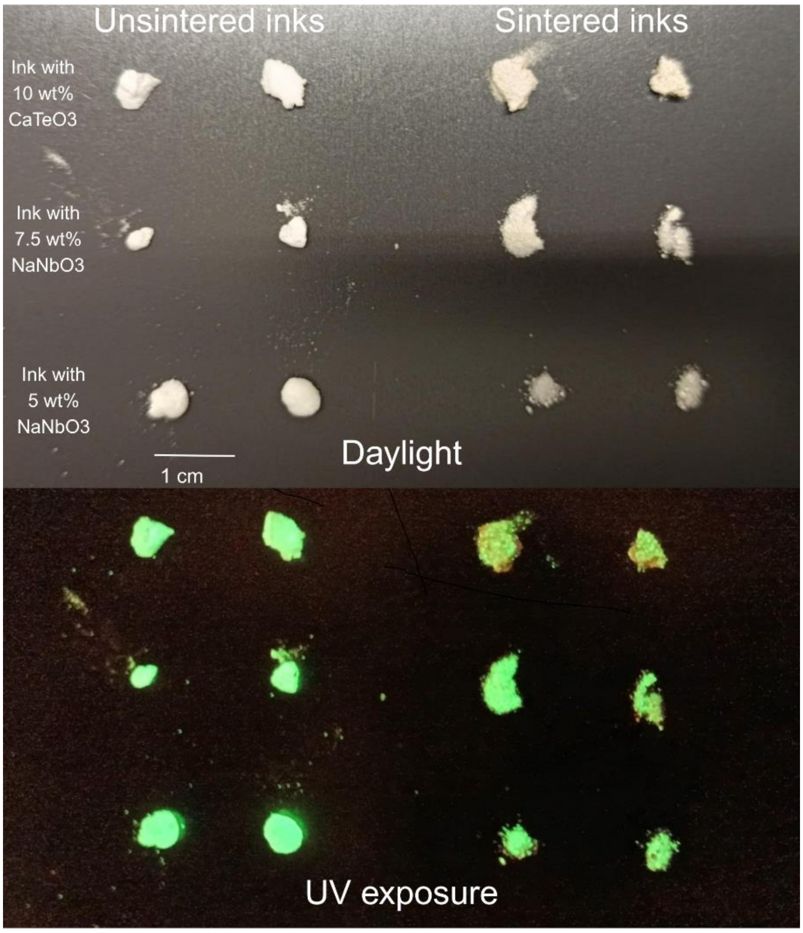

Figure 13: 3D printing inks under daylight and under UV exposure.

After sintering, structural differences between the inks became evident. The ink containing $CaTeO_3$ remained intact and retained its shape, whereas both $NaNbO_3$ crystals-containing inks were brittle and began to fragment under minor impacts. This behavior is likely attributed to the larger particle size of the synthesized $NaNbO_3$ compared to $CaTeO_3$, which may have hindered the effective incorporation of upconverter particles into the glass matrix during sintering.

The UC spectra of the inks prior to and after sintering are presented in Figure 14.

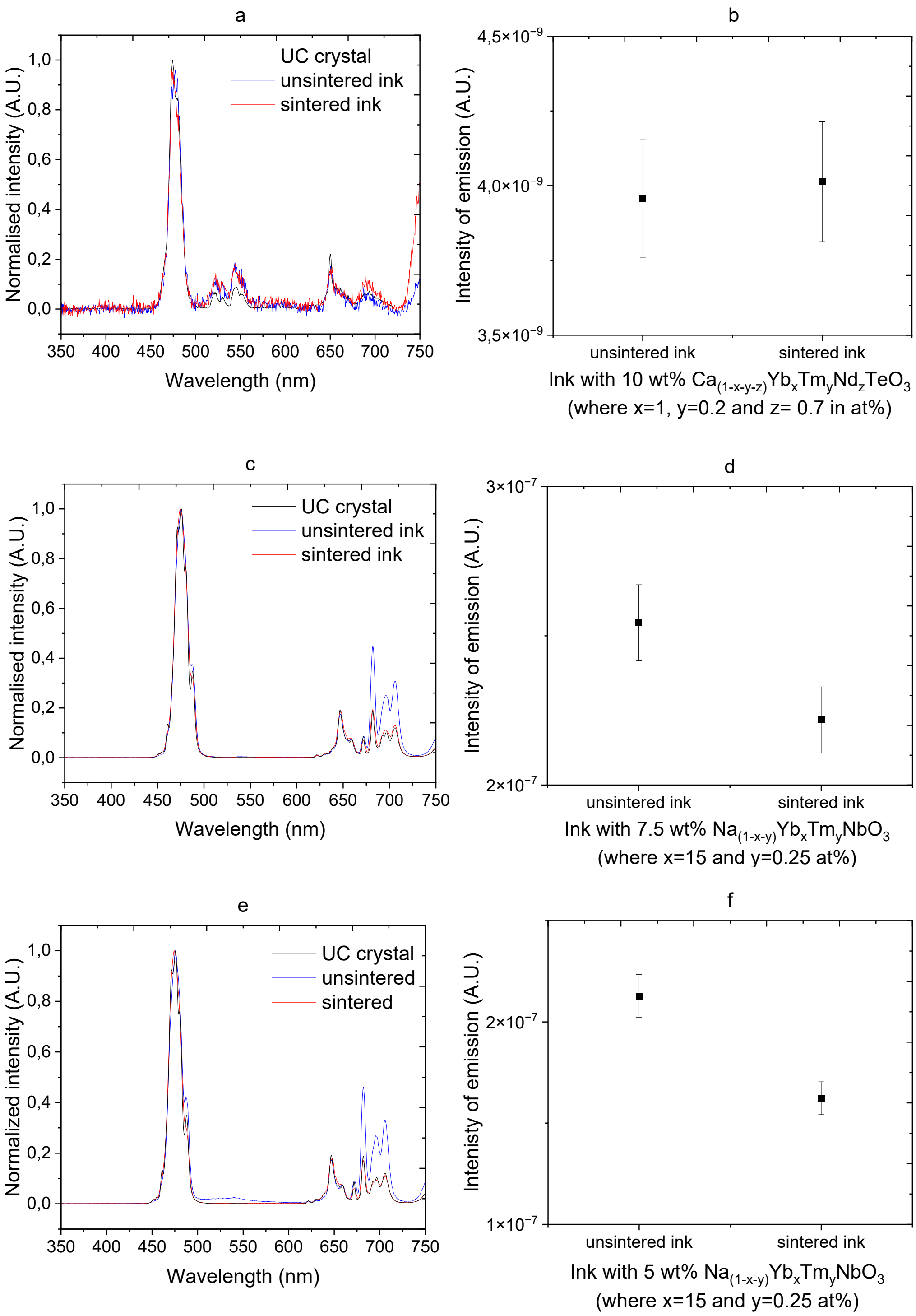

Figure 14: Normalised emission spectra (a, c and e) and intensity of the emission at 475nm (b, d and f) of the investigated 3D printing inks prior to and after sintering under 980 nm excitation.

No change in the shape of the upconversion emission is observed after embedding the crystals in the ink, except for the red emissions which might be related to some luminescence from the organic precursors (Pluronic ®). As observed in Figure 14b, d and f, the sintering process has no noticeable impact on the upconversion properties.

The inks were charged using 980 nm excitation for 10 minutes. The ink with 10 wt% $CaTeO_3$ showed a much weaker green afterglow—or none at all—as it was neither visible to the naked eye nor captured by a phone camera. This result aligns with the weaker blue upconversion performance of $CaTeO_3$ compared to $NaNbO_3$. In contrast, both $NaNbO_3$-based inks demonstrated a sufficiently strong green afterglow to be observed visually, although still not detectable by camera. However, since the structure of the inks with $NaNbO_3$ were not as stable as that of the ink with $CaTeO_3$, this highlights a critical trade-off between luminescence performance and mechanical integrity. While $NaNbO_3$ provided stronger upconversion and afterglow properties, its larger particle size and poor integration into the glass matrix during sintering likely contributed to increased brittleness and reduced structural reliability.

5. CONCLUSION

In this study, new luminescent bioactive scaffolds designed to emit long-lasting green afterglow upon near-infrared (NIR) excitation were developed, addressing the dual challenges of providing structural support and enabling localized photonic activation for potential biomedical applications. The research combined the synthesis of rare-earth (RE) doped upconversion (UC) crystals, the integration of persistent luminescence (PeL) phosphors, and the fabrication of bioactive glass scaffolds using advanced additive manufacturing techniques.

Solid-state synthesis methods produced two types of upconverter crystals— $Ca_{(1-x-y-z)}Yb_xTm_yNd_zTeO_3$ (where x=1, y=0.2 and z= 0.7 in at%) and $Na_{(1-x-y)}Yb_xTm_yNbO_3$ (where x=0.5-20 and y=0.25 at%). Structural analyses confirmed suc-cessful crystal formation, with XRD patterns matching reference data, though $NaNbO_3$ samples exhibited secondary phases at high dopant concentrations. Optical characterization revealed that $NaNbO_3$ crystals demonstrated stronger blue upconversion, particularly at 15 at% Yb^{3+}, whereas $CaTeO_3$ crystals exhibited weaker emission under 980 nm excitation but remained functional at 808 nm. These findings confirmed the critical role of dopant balance and host lattice properties in achieving efficient energy trans-fer and high upconversion intensity.

To enable green afterglow, optimized UC crystals were combined with $SrAl_2O_4$:Eu^{2+}, Dy^{3+} phosphors and a 1393B20 bioactive glass matrix to produce composite inks suitable for scaffold fabrication. Despite successful ink preparation, extrusion-based 3D printing was partially limited by nozzle clogging caused by large particle sizes. Nonetheless, scaffolds and ink samples demonstrated visible green afterglow under NIR excitation, confirming that the UC emission was sufficient to recharge PeL phosphors. These findings suggest that afterglow intensity strongly depends on the upconversion efficiency of the crystals in the glass matrix. This also implies that the emission brightness is insufficient for camera detection, underlining the necessity of optimizing material properties—such as dopant concentration or trap state density—to achieve higher quantum efficiency for practical applications.

Overall, the research validates the feasibility of integrating UC and PeL functionalities into bioactive scaffolds, offering a pathway toward multifunctional implants capable of supporting tissue regeneration while enabling light-triggered biomedical functions, such as localized nitric oxide release for infection eradication. However, the study also revealed key limitations, including the size control of UC crystals, ink rheology optimization, and the need for improved sintering protocols to preserve both mechanical properties and luminescent efficiency.

Future work should prioritize optimizing the size and size distribution of UC crystals, refining 3D printing parameters for reliable fabrication, and enhancing the luminescence-to-mechanical performance balance. Additionally, comprehensive biological evaluations, including in vitro cytocompatibility, degradation behavior, and long-term luminescence stability, are essential for clinical translation. The findings presented herein establish a solid foundation for further advancements in multifunctional photonic scaffolds and contribute to the evolving field of bioactive materials for regenerative medicine.

6. REFERENCES

[AD, 2024] S. AD, P. SPA, J. Naveen, T. Khan, S. Khahro. Advancement in biomedical implant materials-a mini review. Front Bioeng Biotechnol. 2024 Jul 3;12:1400918;

[Ah, 2010] K. Ahrar, A. Gowda, S. Javadi, A. Borne, M. Fox, R. McNichols, JU. Ahrar, C. Ste-phens, RJ. Stafford. Preclinical assessment of a 980-nm diode laser ablation system in a large animal tumor model. J Vasc Interv Radiol. (2010) 555-61;

[Al, 2016] Alaribe, F.N., Manoto, S.L. & Motaung, S.C.K.M. Scaffolds from biomaterials: advantages and limitations in bone and tissue engineering. Biologia 71 (2016), 353–366;

[Al, 2009] Alvarez K, Nakajima H. Metallic Scaffolds for Bone Regeneration. Materials (Basel). 2009 Jul 23;2(3):790–832;

[Ar, 2022] N. Garcia Arango, S. Vuori, H. Byron, D. Van der Heggen, P.F. Smet, M. Lastusaari, L. Petit, Near-infrared rechargeable glass-based composites for green persistent luminescence, Journal of Alloys and Compounds, (2022), Volume 927;

[Ba, 2014] G. BaoLin, PX. Ma. Synthetic biodegradable functional polymers for tissue engineering: a brief review. Sci China Chem. (2014) 490-500;

[Ba, 2018] Bagheri, A., Li, Z., Boyer, C., & Lim, M. NIR/blue light emission optimization of $NaY_{1-(x+y)}Yb_xF_4:Tm_Y$ upconversion nanoparticles via Yb^{3+}/Tm^{3+} dopant balancing. Dalton Transactions, 47(26) (2018), 8629–8637;

[Bh, 2022] Bhushan, S.; Singh, S.; Maiti, T.K.; Sharma, C.; Dutt, D.; Sharma, S.; Li, C.; T. Eldin, E.M. Scaffold Fabrication Techniques of Biomaterials for Bone Tissue Engineering: A Critical Review. Bioengineering (2022), 9, 728;

[Bo, 2012] Bose, S., Vahabzadeh, S., & Bandyopadhyay, A. Bone tissue engi-neering using 3D printing. Materials Today, (2012) 16(12), 496–504;

[Ca, 2021] V. Cannillo, L. Pawlowski, S. Fiorilli, and E. Bernardo. Editorial: Bioc-eramics and/or Bioactive Glass-Based Composites. Front. Mater. (2021) 8:738931;

[Ca, 2022] Z. Cao, S. Dong, S. Shikao, J. Wang, L. Fu, Solid state reaction preparation of an efficient rare-earth free deep-red $Ca_2YNbO6:Mn^{4+}$ phosphor, Journal of Solid State Chemistry, 122840, (2022) Volume 307;

[Ch, 2002] Chen, G., Ushida, T. and Tateishi, T. (2002), Scaffold Design for Tissue Engineering. Macromol. Biosci., 2 (2002): 67-77;

[Ch, 2014] G. Chen, H. Qiu, N. Prasad, and X. Chen; Upconversion Nanoparticles: Design, Nanochemistry, and Applications in Theranostics; Chemical Reviews (2014) 114 (10), 5161-5214;

[Co, 2015] Cox, S.C, Thornby, J.A., Gibbons, G.J., Williams, M.A, Mallick, K.K. 3D printing of porous hydroxyapatite scaffolds intended for use in bone tissue engineering applications, Material Science and Engineering: (2015) C. 47, 237-247;

[Co, 2021] N. Collins, G. Ren, K. Young, S. Pina, L. Reis, J. Miguel; Scaffold Fabrication Technologies and Structure/Function Properties in Bone Tissue Engineering; (2021);

[CT, 2014] J. CT, G. AJ. Scaffold-based anti-infection strategies in bone repair. Ann Biomed Eng. (2014);43(3):515-28;

[Da, 2023] A. Dasan, A. Chandrasekar. Special Issue: Bioceramics, Bioglasses, and Gels for Tissue Engineering. Gels. (2023); 9(7):586;

[DD, 2008] T. DD, R. LA, I. JS, W. Flores-Santana, S. CH, S. Donzelli, P. Hussain, C. Vecoli, N. Paolocci, S. Ambs, C. CA, H. CC, R. DD, W. DA. The chemical biology of nitric oxide: implications in cellular signaling. Free Radic Biol Med. (2008) ;45(1):18-31.

[De, 2017] P. Deb, B. Deoghare, A. Borah, E. Barua, SD. Lala, Scaffold Development Using Biomaterials: A Review, Materials Today: Proceedings, 5, 2, (2018), 12909-12919;

[DM & MP, 2020] S. DM and B. MP, Quantitative Modeling Extends the Antibacterial Activity of Nitric Oxide. Front. Physiol. (2020) 11:330;

[DO, 2012] S. DO, C. JS, N. JD, F. AJ. The potential of nitric oxide releasing therapies as antimicrobial agents. Virulence. (2012); 3(3):271-9;

[Fa, 2022] J. Fan, K. Abedi-Dorcheh, AS. Vaziri, F. Kazemi-Aghdam, S. Rafieyan, M. Sohrabinejad, M. Ghorbani, FR. Adib, Z. Ghasemi, K. Klavins, V. Jahed. A Review of Recent Advances in Natural Polymer-Based Scaffolds for Musculoskeletal Tissue Engineering. Polymers (Basel). (2022) 14(10):2097;

[Fu, 2011] Q. Fu, E. Saiz, MN. Rahaman, AP. Tomsia. Bioactive glass scaffolds for bone tissue engineering: state of the art and future perspectives. Mater Sci Eng C Mater Biol Appl. (2011);31(7):1245-1256;

[Gh, 2024] S. Ghanavati, E. Santos Magalhaes, C. Nguyen, B. Bondzior, M. Lastusaari, J.N. Anker, A. Draganski, L. Petit, J. Massera, Biophotonic composite scaffolds for controlled nitric oxide release upon NIR excitation, Materials & Design, 247 (2024), 113369;

[Ha, 2020] V. Havasi, D. Tátrai, G. Szabó, E. Varga, A. Erdőhelyi, G. Sipos, Z. Kónya, Á. Kukovecz, On the effects of milling and thermal regeneration on the luminescence properties of Eu^{2+} and Dy^{3+} doped strontium aluminate phosphors, J. Lumin. 219 (2020) 116917;

[Ja, 2016] A. Jain, A. Kumar, S.J. Dhoble, D.R. Peshwe, Persistent luminescence: An insight, Renewable and Sustainable Energy Reviews, 65 (2016), Pages 135-153;

[Ja, 2012] MK. Jayakumar, NM. Idris, Y. Zhang. Remote activation of biomolecules in deep tissues using near-infrared-to-UV upconversion nanotransducers. Proc Natl Acad Sci U S A. (2012);

[Ji, 2022] L. Jiang, D. Chen, Z. Jin, C. Xia, Q. Xu, M. Fan, Y. Dai, J. Liu, Y. Li, Q. He, Light-triggered nitric oxide re-lease and structure transformation of peptide for enhanced intratumoral retention and sensitized photodynamic therapy, Bioactive Materials, 12, (2022) 303-313;

[Ji, 2018] PP. Jignesh, HP. Parsotam, 3 - Characterization, testing, and reinforcing materials of biodegradable composites, In Woodhead Publishing Series in Composites Science and Engineering, Biodegradable and Biocompatible Polymer Composites, Woodhead Publishing, (2018), 55-79;

[Ka, 2023] MH. Kaou, M. Furkó, K. Balázsi, C. Balázsi. Advanced Bioactive Glasses: The Newest Achievements and Breakthroughs in the Area. Nanomaterials (Basel), (2023);13(16):2287;

[Ku, 2022] A. Kumar, A. Jacob. Techniques in scaffold fabrication process for tissue engineering applications: A review. J Appl Biol Biotech (2022); 10(03):163–176;

[Ku, 2004] Kurumada, Ki., Robinson, B.H. Viscosity studies of pluronic F127 in aqueous solution. In: Miguel, M., Burrows, H. (eds) Trends in Colloid and Interface Science XVI. Progress in Colloid and Polymer Science, vol 123 (2004);

[La, 2022] S. Lamnini, H. Elsayed, Y. Lakhdar, F. Baino, F. Smeacetto, E. Bernardo, Robocasting of advanced ceramics: ink optimization and protocol to predict the printing parameters - A review, Heliyon, 8, 9 (2022), e10651;

[Lo, 2015] Q. Long, C. Wang, Y. Li, J. Ding, X. Wang, Y. Wang, Solid state reaction synthesis and photoluminescence properties of Dy^{3+} doped $Ca_3Sc_2Si_3O_{12}$ phosphor, Materials Research Bulletin, 71, (2015), 21-24;

[Lu, 2022] JO. Lundberg, E. Weitzberg. Nitric oxide signaling in health and disease, Cell, Volume 185, Issue 16, (2022) 2853-2878;

[Ma, 2008] PX. Ma, Biomimetic materials for tissue engineering, Advanced Drug Delivery Reviews, 60, 2 (2008), 184-198;

[Mc, 2002] H. McGraw, x-ray diffraction. (n.d.) Concise Encyclopedia of Physics. (2002);

[Me, 2023] A. Mesaros, Luminescent Materials: Synthesis, Characterization and Application. Appl. Sci. (2023), 13, 11221;

[Me, 2008] M. Meinhardt, R. Krebs, A. Anders, U. Heinrich, & H. Tronnier. Wavelength-dependent penetration depths of ultraviolet radiation in human skin. Journal of Biomedical Optics, (2008) 13(4);

[Na, 2018] S. Nan , Z. Bo , Y. Long , H. Jinshu , Z. Qinyuan; Understanding the Role of Yb^{3+} in the Nd/Yb Coupled 808-nm-Responsive Upconversion; Frontiers in Chemistry 6, (2019);

[Ng, 2022] C. Nguyen, Development of biophotonic glass-based materials for biomedical applications. Bachelor of Science Thesis, Tampere University (2022);

[Oj, 2018] N. Ojha, H. Nguyen, T. Laihinen, T. Salminen, M. Lastusaari, L. Petit, Decomposition of persistent luminescent microparticles in corrosive phosphate glass melt, Corrosion Science, 135 (2018), 207-214;

[OB, 2011] FJ. O'Brien, Biomaterials & scaffolds for tissue engineering, Materials Today, 14, 3 (2011), 88-95;

[Pr 2017] Prakasam, Mythili & Madalina, Laura & Piticescu, Roxana & Largeteau, Alain; Fabrication Methodologies of Biomimetic and Bioactive Scaffolds for Tissue Engineering Applications. (2020);

[Pr, 2025] K. Prasad, AA. Sharma, PP. Pradhan, M. Rakshita, D. Haranath. Unveiling the potential of a self-activated BCNO afterglow phosphor for superior visibility in extremely low-light environments. RSC Adv. (2025);15(30):24367-24380.

[Qi, 2024] L. Qin, S. Yang, C. Zhao. Prospects and challenges for the application of tissue engineering technologies in the treatment of bone infections. Bone Res 12, 28 (2024);

[Sz, 2024] A. Szczodra, A. Houaoui, T. Salminen. Pore graded borosilicate bioactive glass scaffolds: in vitro dissolution and cytocompatibility. J Mater Sci: Mater Med 35, 17 (2024);

[Te, 2023] B. Tegze, G. Tolnai, D. Hessz. Effect of heat treatment temperature on the morphology and upconversion properties of LaF_3:Yb,Er nanoparticles. J Therm Anal Calorim 148, (2023) 10795–10802;

[Ti, 2020] Y. Tian, X. Li, R. Shen, C. Han, X. Wang, S. Xu, L. Cheng, J. Sun, J. Zhang, X. Zhang, B. Chen. Laser-induced thermal effect and the role of Nd^{3+} in $Tm^{3+}/Yb^{3+}/Nd^{3+}$ triply doped $LaNbO_4$ upconversion phosphors under 808 nm excitation, Journal of Luminescence, (2020) Volume 223;

[Va, 2023] L. Vaiani, A. Boccaccio, AE. Uva, G. Palumbo, A. Piccininni, P. Guglielmi, S. Cantore, L. Santacroce, IA. Charitos, A. Ballini. Ceramic Materials for Biomedical Applications: An Overview on Properties and Fabrication Processes. J Funct Biomater. 2023 Mar 4;14(3):146;

[Va, 2017] M. Vandenhaute, "Stability of Pluronic® F127 bismethacrylate hydro-gels," Polymer Degradation and Stability, (2017).

[Ve, 2022] O. Vesvoranan, A. Anup, KR. Hixon. Current Concepts and Methods in Tissue Interface Scaffold Fabrication. Biomimetics (Basel). (2022);7(4):151;

[Vy, 2020] C. Vyas, G. Ates, E. Aslan, J. Hart, B. Huang, and P. Bartolo; Three-Dimensional Printing and Electrospinning Dual-Scale Polycaprolactone Scaffolds with Low-Density and Oriented Fibers to Promote Cell Alignment; 3D Printing and Additive Manufacturing 7:3, (2020) 105-113;

[Wa, 2025] B. Wan, C. Wu, Z. Man, Z. Zhang, MV. Swain, Q. Li. On fracture modelling of implantable load-bearing bioceramic structures and its state of the art, Acta Biomaterialia, 2025;

[Wu, 2025] Wu, S., Qin, F., & Meng, Y. The application and challenges of antimicrobial drug-loaded scaffold materials for the treatment of bone infections. *Nanoscale Horizons*, (2025) 10(8), 456-468;

[Xi, 2016] Q. Xiao. "Dynamically Tuning the Up-conversion Luminescence of $NaNbO_3:Er^{3+},Yb^{3+}$ Nano-crystals by Magnetic Field." Scientific Reports, 6, (2016) 31327;

[Ye, 2020] ZQ. Ye, SG. Xiao, XL. Yang. Up-conversion of $Nd^{3+}/Yb^{3+}/Tm^{3+}$ tri-doped CaTeO3 compound under excitation of 808 nm. Rare Metals. (2020) 40;

[Zh, 2020] E. Zhou, H. Knox, C. Reinhardt, G. Partipilo, J. Chan. Near-infrared photoactivatable nitric oxide donors with photoacoustic readout. Methods Enzymol. (2020) 641:113-147.